

NANO EXPRESS

Open Access



Eggshell Membrane-Templated MnO_2 Nanoparticles: Facile Synthesis and Tetracycline Hydrochloride Decontamination

Qi Wang^{1†} , Chunlei Ma^{1†}, Jianke Tang¹, Cuihong Zhang¹ and Lihua Ma^{2,3*}

Abstract

Taking advantages of reticular proteins and reductive groups on the surface, eggshell membrane (ESM) was selected to synthesize MnO_2 nanoparticles from potassium permanganate through a super simple way in which ESM acted as both template and reductant. This process avoided harsh reaction conditions or complicated aftertreatments and thus owned the merits of green synthesis, handy operation, low cost, and easy purification. The ESM-templated MnO_2 nanoparticles (MnO_2 NPs/ESM) were characterized, and the content of nanomaterials on the template was tested. MnO_2 NPs/ESM showed a good capacity for decontamination of tetracycline hydrochloride (TCH). The macroscopical materials can be separated easily by taking the membrane out to stop the degradation instead of centrifugation or filtration. It was studied that 72.27% of TCH (50 mg/L) was decontaminated in 20 min by 0.1920 g/L MnO_2 nanoparticles, and removal efficiency could reach 83.10% after 60 min under buffered condition. The kinetics was studied with or without buffer, and it was concluded that the degradation process followed a pseudo-second-order model. The facile synthesis of materials and effective degradation would facilitate the nano- MnO_2 -based decontamination applications.

Keywords: MnO_2 nanoparticles, Eggshell membrane, Tetracycline, Decontamination

Background

Pharmaceuticals and personal care products (PPCPs) are a kind of emerging water pollutions and are concerned closely by researchers in consideration of ecology and human health [1–5]. Antibiotics as a medicine to treat and prevent bacterial infections are used worldwide, accompanying with which upsetting risks to the environment have gradually appeared [6]. As a representative, tetracycline (TC) medicines have been used in veterinary science and aquaculture for years [7]. However, TCs can hardly be degraded in the environment and thus persist for a long time [8, 9], which lead to a various negative influence on the ecosystem or human health [10–13]. Therefore, screening a facile and effective way to decontaminate TC-contaminated water has become a hotspot

of research. One promising technique may be the assistance of manganese dioxide nanomaterials.

Manganese dioxide nanomaterials have been extensively studied owing to their unique merits of high surface area, tunable structure, catalytic oxidation activity, and eco-harmless [14, 15]. Therefore, nano- MnO_2 -based applications have covered various fields ranging from catalysis [16, 17], sensors [18, 19], and capacitors [20, 21] to drug delivery [22, 23] and cancer therapy [24, 25]. By the same token, MnO_2 nanomaterials with adsorption and oxidation properties have applied to wastewater treatment. Water pollutants including heavy ions [26], organic dyes [27], and phenols [28] treated by MnO_2 nanomaterials were reported. Meanwhile, antibiotics such as levofloxacin [29], ciprofloxacin [30], norfloxacin [31], sulfamethoxazole [32], sulfadiazine [33], cefazolin [34], lincosamide [35], and TCs [36, 37] have been successfully decontaminated through MnO_2 treatment. Specific to TC antibiotics, highly porous MnO_2 nano-sheets were utilized to degrade tetracycline, and pH, temperature, and dose-based kinetics were investigated

* Correspondence: wangqitit@163.com; lihuam@bcm.edu; mal@uhcl.edu

[†]Qi Wang and Chunlei Ma contributed equally to this work.

¹Chemistry and Chemical Engineering Department, Taiyuan Institute of Technology, Taiyuan 030008, Shanxi, China

²NMR and Drug Metabolism Core, Baylor College of Medicine, One Baylor Plaza, Houston, TX 77030, USA

Full list of author information is available at the end of the article

[38]. A MnO_2 -based scheme was applied to remove tetracycline hydrochloride (TCH) and As(III) simultaneously, and the interactive effect on arsenic and antibiotics during MnO_2 treatment was studied [39]. Degradation of tetracycline antibiotics by MnO_2 was performed, and transformation kinetics and pathways were reported [40]. Though high removal efficiency of TCs was obtained in the abovementioned works, however, the degradation operation usually involved in the centrifugation or filtration in order to separate the material from antibiotics solutions, which took much of the treatment time and made the process complicated.

Eggshell membrane (ESM) as a unique biomaterial with extraordinary properties has been utilized in materials science extensively [41]. The main composition of fiber in ESM is a protein which endows ESM the ability to bind metal. Noble metal nanomaterials like Ag NPs and Au NPs were successfully synthesized using ESM as a template [42–44]. In addition, metal oxide nanomaterials such as ZnO [45], Co_3O_4 [45], PbO [45], Mn_3O_4 [46], and TiO_2 [47] were also prepared through ESM templating, which made the synthesis facile and under control and therefore provided a novel path for the synthesis of metal or metal oxide nanoparticles.

In this work, eggshell membrane-templated MnO_2 nanoparticles (MnO_2 NPs/ESM) were synthesized simply and quickly by a bio-templating method. Eggshell membrane played dual roles as a template and a reductant making nanoparticles dispersed uniformly on the macroscopical membranes. Combining the oxidizing MnO_2 nanoparticles with the easy-to-manipulate membrane, MnO_2 NPs/ESM were further applied to tetracycline hydrochloride decontamination, in which nanomaterials could be separated easily by simply taking out of solutions.

Methods

Materials and Apparatus

Deionized water with a conductivity of $18.2 \text{ M}\Omega \text{ cm}^{-1}$ was used in this experiment from a water purification system (ULUPURE, Chengdu, China). Potassium permanganate (KMnO_4 , $M_w = 158.03$), MnO_2 powder, and other reagents were at least of analytical grade and purchased from Kemiou Chemical Co. Ltd. (Tianjin, China). Tetracycline hydrochloride (TCH, USP grade) and glutathione (GSH, 98%) were purchased from Aladdin Reagents Company (Shanghai, China). Eggshell membrane (ESM) was peeled off carefully from a fresh eggshell which is obtained from Hongye student mess hall of Taiyuan Institute of Technology. PBS buffer solutions (0.2 M, pH = 7.0) were prepared by mixing 39 mL NaH_2PO_4 solution (0.2 M) and 61 mL Na_2HPO_4 solution (0.2 M), and PBS solutions with different pH values were prepared by titrating the abovementioned solution

with sodium hydroxide or hydrochloric acid solution (both concentrations were 0.2 M) to the required pH values.

Scanning electron microscopy (SEM) of MnO_2 NPs/ESM was carried out on a Quanta 200 FEG scanning electron microscope for the morphology observation. Transmission electron microscopy (TEM) and high-resolution transmission electron microscopy (HRTEM) of MnO_2 NPs were performed on a Tecnai-G20 transmission electron microscope. The size distribution of as-prepared MnO_2 NPs was obtained at a laser particle sizer (Malvern Nano-ZS90). X-ray photoelectron spectroscopy (XPS) was collected on an AXIS ULTRA DLD electron spectrometer (Kratos) with monochromatic Al K α radiation for the surface composition and chemical state test of the product. Thermogravimetry (TG) analysis of ESM and MnO_2 NPs/ESM was measured in air at a heating rate of $10^\circ\text{C}/\text{min}$ on a Rigaku TG thermal analyzer (Rigaku Co. Japan). Fourier transform infrared spectroscopy (FTIR) from 4000 to 400 cm^{-1} of ESM and MnO_2 NPs/ESM was recorded in KBr discs on a Tensor II FTIR spectrometer (Bruker, Germany), and the spectra were processed through deconvolution. The ultraviolet-visible (UV-vis) absorption spectra of TCH were recorded on a TU-1901 UV-vis spectrophotometer (Puxi, China).

Synthesis of ESM-Templated MnO_2 Nanoparticles

The eggshell membrane-templated MnO_2 nanoparticles (MnO_2 NPs/ESM) were synthesized through a straightforward and facile method. In a typical process, the eggshell membrane was firstly peeled off from a fresh eggshell manually and washed ten times with deionized water to remove the needless egg white. After drying under room temperature, the clean ESM was then cut into slices with 5 mg weight each. Upon synthesis, ten slices of ESM were soaked into 20 mL KMnO_4 solution (1 mmol/L) and the open system kept stirring under room temperature. Thirty-five minutes later, the ESM slices were taken out and washed ten times with deionized water to remove the redundant solution. At last, the obtained membranes were dried and stocked at room temperature for further characterization and use.

Decontamination of TCH

The decontamination of TCH was performed by adding MnO_2 NPs/ESM into the TCH solutions simply and stirred under room temperature. Twenty slices of MnO_2 NPs/ESM were placed into 15 mL TCH solutions (50 mg/L) which were diluted by PBS buffer solutions and kept stirring for 60 min. The UV-vis spectra of TCH solutions after treatment were recorded immediately at room temperature. All of the absorption intensities of TCH measurement were set at a wavelength of 358 nm.

The removal efficiency (R , %) was calculated using the equation below:

$$R = \frac{C_0 - C}{C_0} \times 100\%$$

where C_0 and C (mg/L) stand for the initial and final concentrations of TCH in the treatment solutions, respectively.

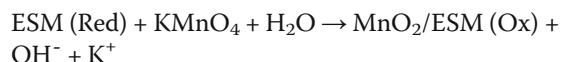
Results and Discussion

Mechanism and Monitoring of MnO_2 NPs/ESM Synthesis

The synthesis of MnO_2 NPs/ESM was performed in an open system with ESM as biotemplate. The eggshell membrane was composed of many fibrous proteins on which lots of reductive groups like $-\text{OH}$, $-\text{NH}_2$, $-\text{SH}$, etc. were interspersed. An in situ redox reaction was triggered once the KMnO_4 was introduced. While MnO_2 was generated, it grew gradually around these active groups. As a consequence, it was dispersed uniformly on the surface of fibrous proteins to form ESM-templated MnO_2 NPs.

Figure 1a displayed the photos of synthesis system at different times, in which purple KMnO_4 solution turned into light brown gradually, and meanwhile, the white ESM slices became brown (Fig. 1b, c). To monitor the

synthetic process, the absorption intensity of KMnO_4 at 525 nm and pH of this system were investigated in Fig. 1d, e. As shown, the absorption intensity of KMnO_4 decreased with time prolonged, and pH, conversely, improved gradually. Two sets of data both showed a platform after 35 min, and therefore, the synthesis time was selected. The increasing of pH was attributed to the formation of $-\text{OH}$ during the reaction and a reaction course was speculated below:



Characterization of MnO_2 NPs/ESM

The morphology of the obtained MnO_2 NPs/ESM was investigated by scanning electron microscopy (SEM) in Fig. 2. Multilayered and intersecting fibrin network was observed in Fig. 2a, b. After further amplification, lots of particles were found uniformly coated on the surface of fibrous proteins. Therefore, it was concluded that ESM acted not only as a reductant but also a template during the synthesis. To further investigate the size of MnO_2 particles, a laser particle sizer test was carried out. In order to rule out the possibility that the particles with 4.8 nm were decomposed proteins, MnO_2 NPs/ESM and

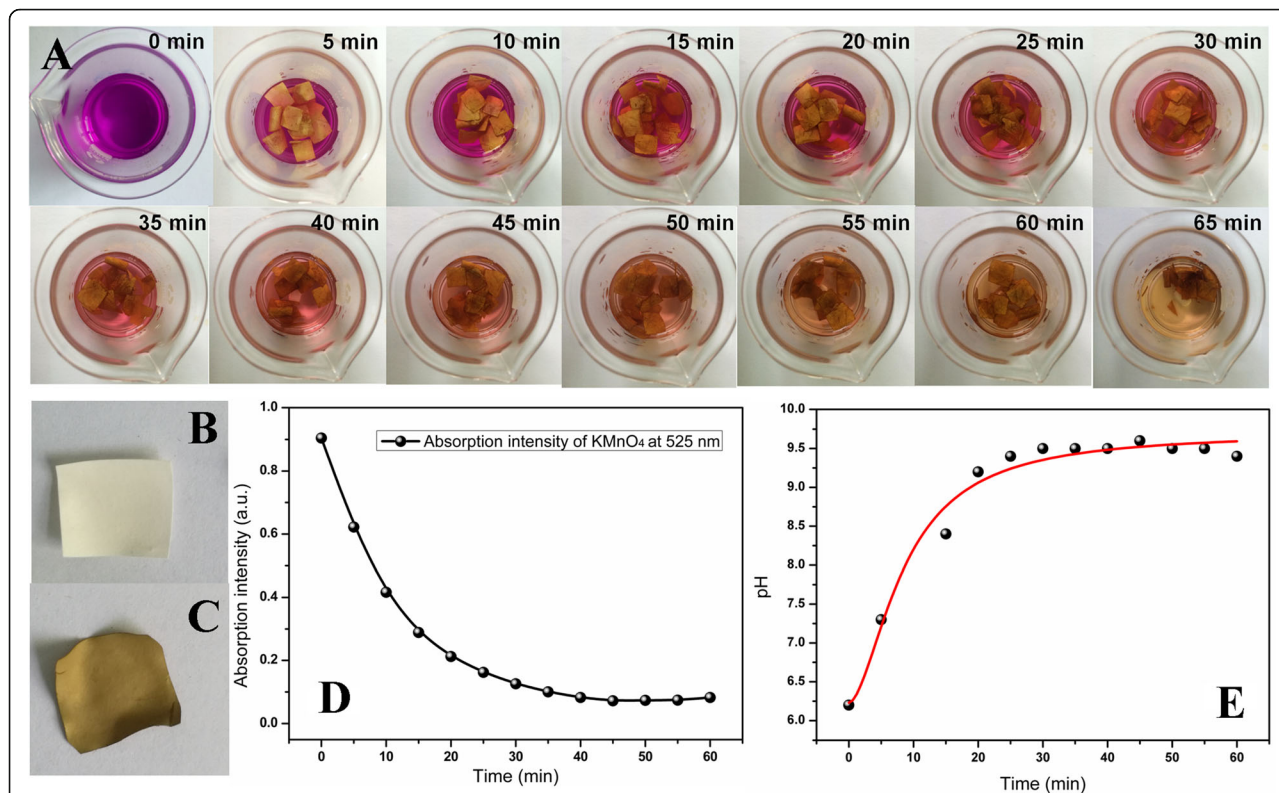


Fig. 1 a The photos of the synthetic system at different times. b The image of ESM slice before the redox reaction. c The image of MnO_2 NPs/ESM. d The absorption intensity of KMnO_4 at 525 nm. e pH of the synthetic system at different times

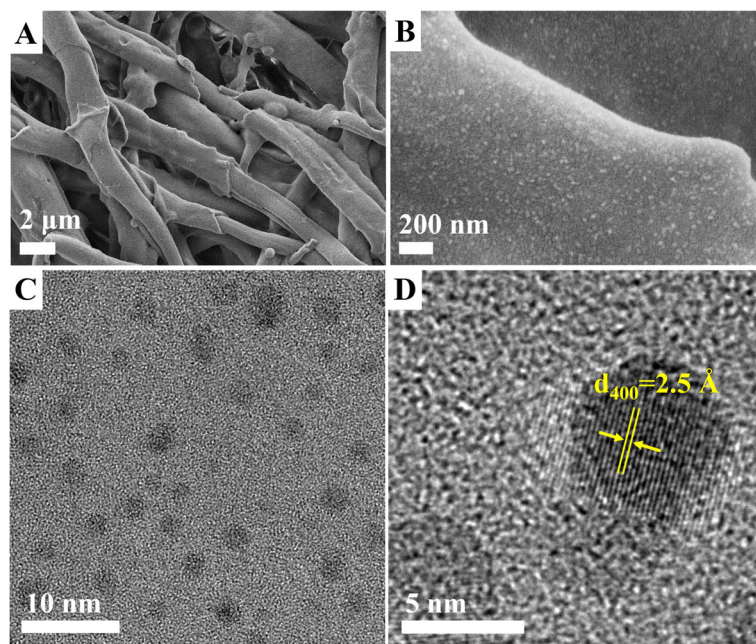


Fig. 2 The SEM images of MnO₂ NPs/ESM with different scale bars (2 μm (a) and 200 nm (b)). The TEM (c) and HRTEM (d) images of MnO₂ NPs, the scale bars were 10 nm and 5 nm, respectively

equal amounts of blank ESM (control) were first placed in NaOH solutions (0.1 M) and boiled for 30 min and then filtered to form solutions to meet the test condition. It was found in Additional file 1: Figure S1 that the average size of MnO₂ NPs was 4.8 nm. The photos of MnO₂ NPs/ESM before and after NaOH treatment were displayed in Additional file 2: Figure S2A. It was obvious that the brown color of the membrane faded evidently while the membrane kept unchanged after NaOH treatment, indicating that the MnO₂ NPs were released from the template. In thinking about the problem that the size of the protein from the eggshell may interfere with the results, the filtrated solutions after NaOH treatment were obtained from both blank ESM and MnO₂ (Additional file 2: Figure S2B) to be colorless and brown, respectively. In addition, the size distribution data of ESM after NaOH treatment displayed an average size of 1.7 nm in Additional file 2: Figure S2C. Therefore, the possibility that the particles with 4.8 nm were decomposed proteins from ESM itself was ruled out. Based on this, TEM was captured after the aforementioned filtrate was dialyzed. As shown in Fig. 2c, spherical nanoparticles were observed and the size was consistent with the one in Additional file 1: Figure S1. The HRTEM image in Fig. 2d indicated a lattice spacing of 2.5 Å that was well coincident with the (400) lattice plane of α-MnO₂ [48].

Besides, X-ray photoelectron spectroscopy (XPS) technique was carried out for the surface composition and elemental analysis of the obtained MnO₂ NPs/ESM. The

full-scan spectrum (Fig. 3a) indicated that the synthesized material was composed of elements Mn 2p, O 1s, N 1s, and C 1s. Element C 1s, N 1s, and partial O 1s came from the template ESM. The partial XPS spectra of Mn 2p and O 1s were measured to study the details. As shown in Fig. 3b, two peaks at 653.8 and 642.0 eV can be assigned to Mn 2p_{1/2} and Mn 2p_{3/2}, respectively. The O 1s spectrum (Fig. 3c) can be divided into three component peaks with binding energy at 532.6, 531.4, and 530.5 eV, which were attributed to H–O–H, Mn–O–H, and Mn–O–Mn, respectively. The above data demonstrated that the as-prepared material was ESM-templated MnO₂ NPs.

To further verify this result, GSH solution was applied to the test thus obtained material inspired by a special reaction between GSH and MnO₂ [49, 50]. As shown in Additional file 3: Figure S3, the brown color of MnO₂ disappeared after soaking into GSH solution for 1 min, indicating that the materials coated on ESM were MnO₂. Furthermore, thermogravimetry (TG) analysis was carried out to measure the mass content of MnO₂ on ESM. The black and red curves in Additional file 4: Figure S4 stood for the mass changes of ESM only and MnO₂ NPs/ESM, respectively. The relative quality of ESM was almost zero at 600 °C indicating that ESM was totally burnt out. However, the relative quality of ESM-templated MnO₂ NPs remained at 2.61% after ESM was burnt out. It was reported that MnO₂ was thermally decomposed at 500 °C and converted into

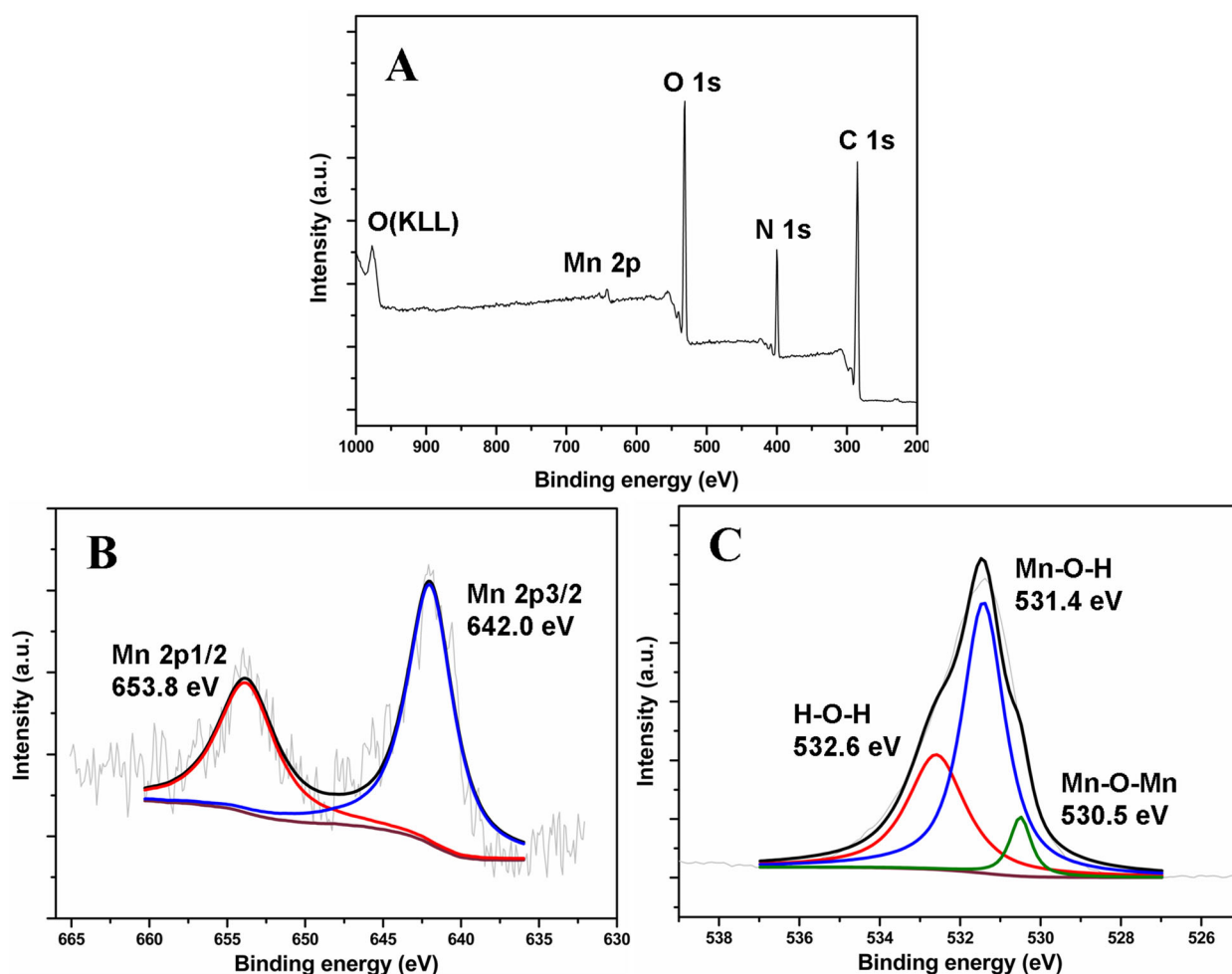


Fig. 3 The XPS (a) full scan, (b) Mn 2p, (c) O 1s spectra of as-prepared MnO₂ NPs/ESM

Mn₂O₃ [51]. Moreover, further thermal decomposition of Mn₂O₃ to Mn₃O₄ occurred above 1000 °C [52]. Therefore, the mass content of 2.61% at 800 °C obtained in this experiment reflected the content of Mn₂O₃. According to the mass conservation of Mn, the original MnO₂ content loading on the ESM was calculated to be 2.88%.

FTIR spectra (Additional file 5: Figure S5) of ESM and MnO₂ NPs/ESM were collected after grinding the materials into powder. The interactions between proteins and nanoparticles mainly involve secondary structure changes, which are reflected on the band of amide I ~ 1650 cm⁻¹ (which may shift a bit) or amide II ~ 1550 cm⁻¹. However, there were no obvious changes of peak position around 1650 or 1550 cm⁻¹ of ESM before and after MnO₂ was involved, which was different from the previously reported results that could demonstrate the structural change of protein [53]. In order to get into the details and avoid missing any minor changes, deconvolution was applied to

these spectra. Even though no observable peaks were shown up around 1650 or 1550 cm⁻¹, a new peak at 506 cm⁻¹ appeared after MnO₂ NPs loading, and it was associated with the characteristic vibrational mode of Mn–O [54].

Mn has various oxidation states, so there are a few types of oxides, such as Mn₂O₃, MnO, and MnO₂. The binding energy of Mn₂O₃ is close to that of MnO₂. In order to examine the oxidation state of Mn in this work, the HRTEM of as-prepared materials was imaged and displayed in Fig. 2d. The lattice spacing of 2.5 Å detected is well coincident with the (400) lattice plane of α-MnO₂ [48]. Moreover, our Mn materials were obtained based on the redox reaction between KMnO₄ and ESM under the neutral condition that favored the formation of MnO₂ instead of other oxidation states [55]. Importantly, as-prepared materials possess the reaction activity with GSH (Additional file 3: Figure S3), which is also a testimonial that the nanoparticle is MnO₂ [49, 50]. It was also

reported that MnO_2 could thermally be decomposed at 500 °C and converted into Mn_2O_3 [51]. The TG curve of the as-prepared materials in Additional file 4: Figure S4 shows an obvious weight loss around 500 °C, indicating the transformation from MnO_2 to Mn_2O_3 , which is another testimony that the oxidation state of Mn is MnO_2 .

TCH Decontamination by MnO_2 NPs/ESM

Taking advantages of oxidative MnO_2 NPs and macroscopical template, MnO_2 NPs/ESM were applied to tetracycline hydrochloride (TCH) decontamination owing to the effective removal and easy operation. Figure 4a displayed the time-dependent absorption intensity of TCH at 358 nm treated by ESM only (black) and MnO_2 NPs/ESM (red). It was shown that absorption intensity kept unchanged in the presence of ESM only. However, it dropped sharply first and flattened out gradually under MnO_2 NPs/ESM treatment. This evident contrast demonstrated the capacity of MnO_2 NPs/ESM for TCH decontamination. Similarly, the UV-vis absorption spectra

of TCH after ESM treatment hardly changed, but the absorption peak at 358 nm decreased obviously after MnO_2 NPs/ESM decontamination (Fig. 4b). Figure 4c investigated the absorption spectra variation of TCH, in which the absorption peak at 270 nm lowered in the first 10 min, but another peak at 358 nm decreased along with time was observed. The time-dependent removal efficiency by MnO_2 NPs/ESM decontamination was calculated in Fig. 4d, and it was found that removal efficiency was 72.27% at 20 min and it can reach 83.10% in 60 min.

Effect of pH and Buffer on TCH Decontamination

The pH played an important role in MnO_2 -based oxidative degradation, and the effect of pH on TCH decontamination in this work was investigated. Figure 5a displayed the absorption intensity of TCH before and after MnO_2 NPs/ESM treatment for 60 min under different pH, and the corresponding removal efficiency was calculated in Fig. 5b. It was demonstrated that the

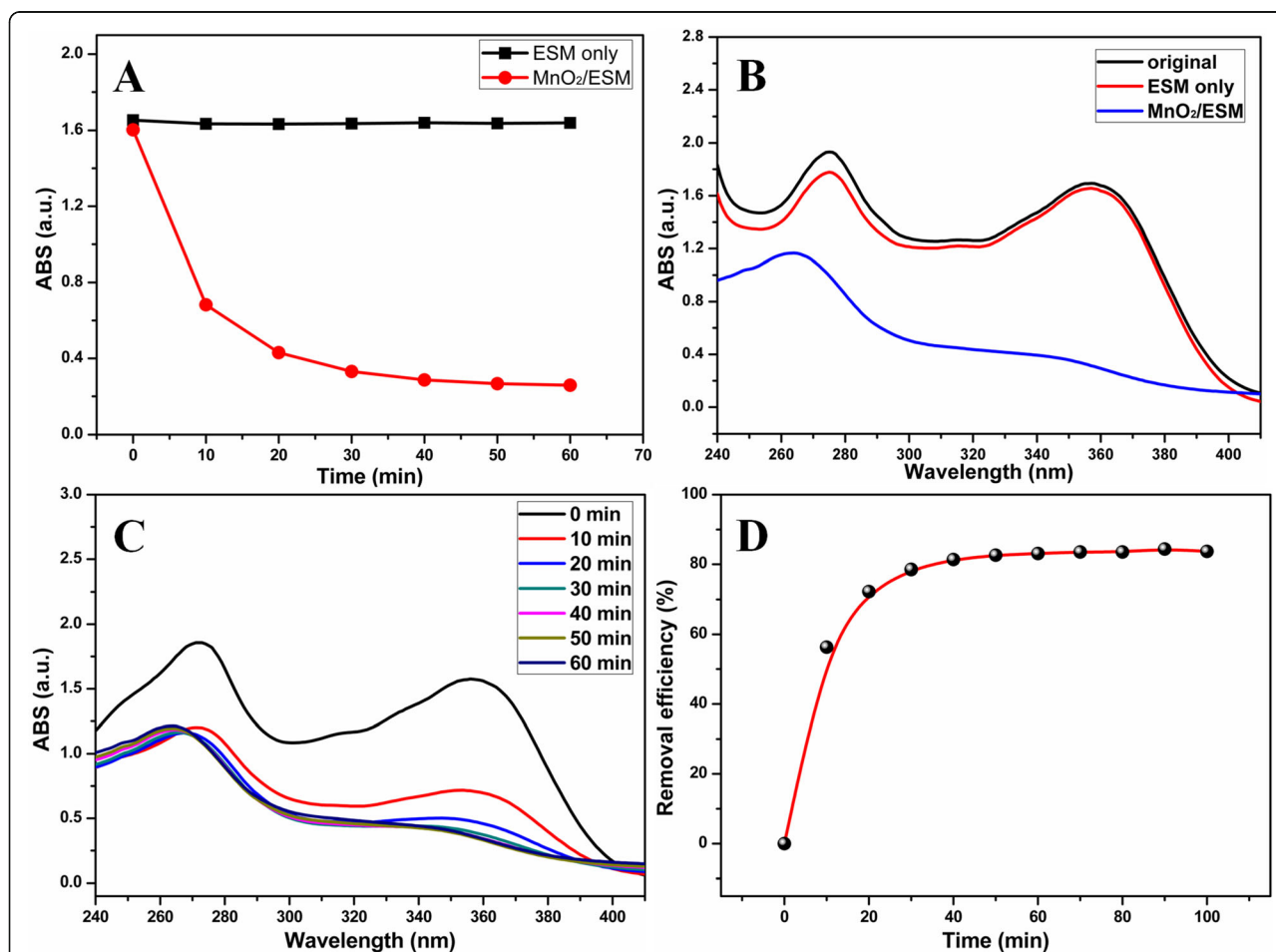
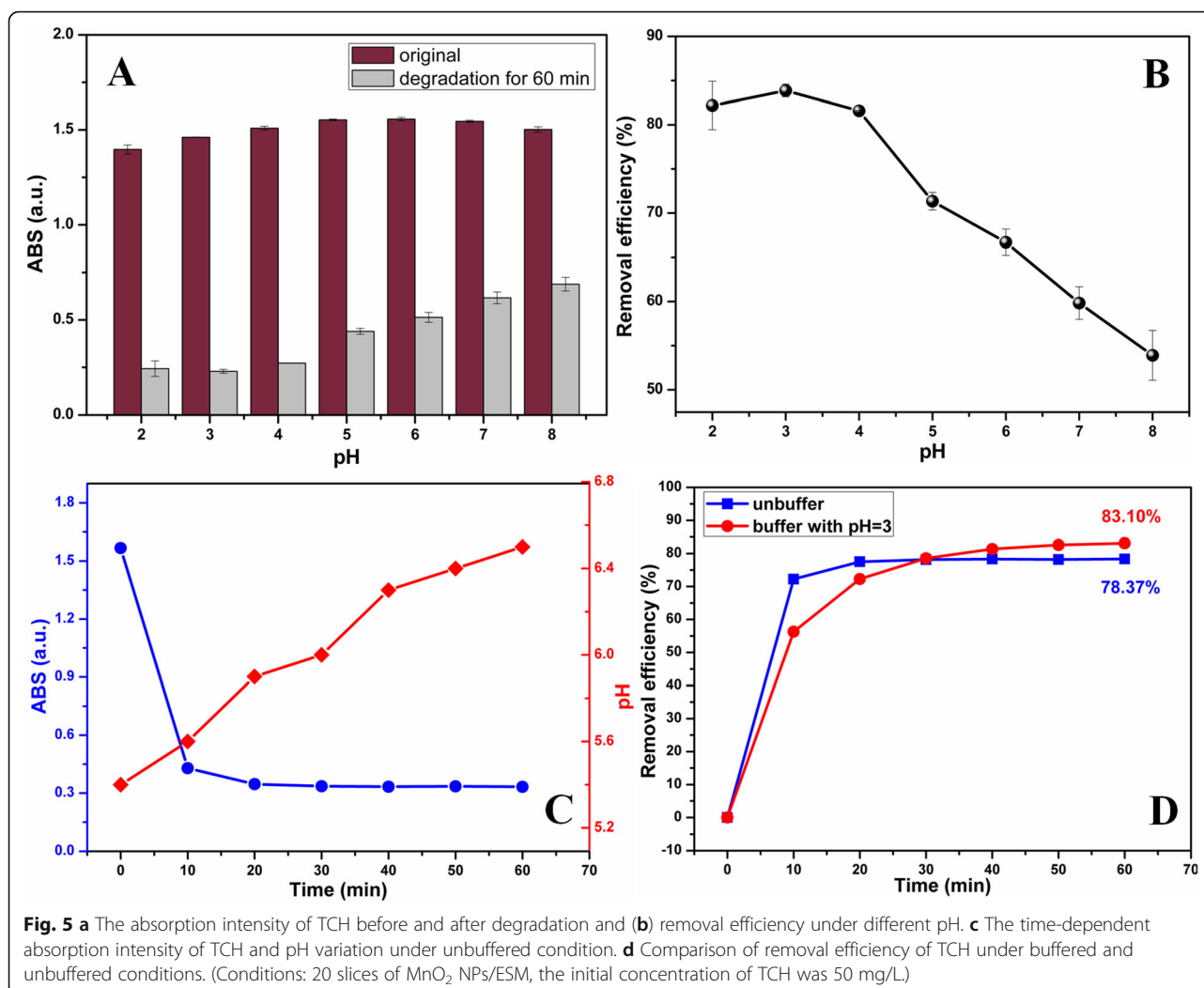


Fig. 4 **a** The time-dependent absorption intensity of TCH by ESM and MnO_2 NPs/ESM treatment. **b** The UV-vis absorption spectra of TCH before and after ESM or MnO_2 NPs/ESM treatment. **c** The time-dependent UV-vis absorption spectra of TCH and **(d)** removal efficiency treated by MnO_2 NPs/ESM. (Conditions: 20 slices of MnO_2 NPs/ESM or ESM, the initial concentration of TCH was 50 mg/L, controlled pH was 3.0)

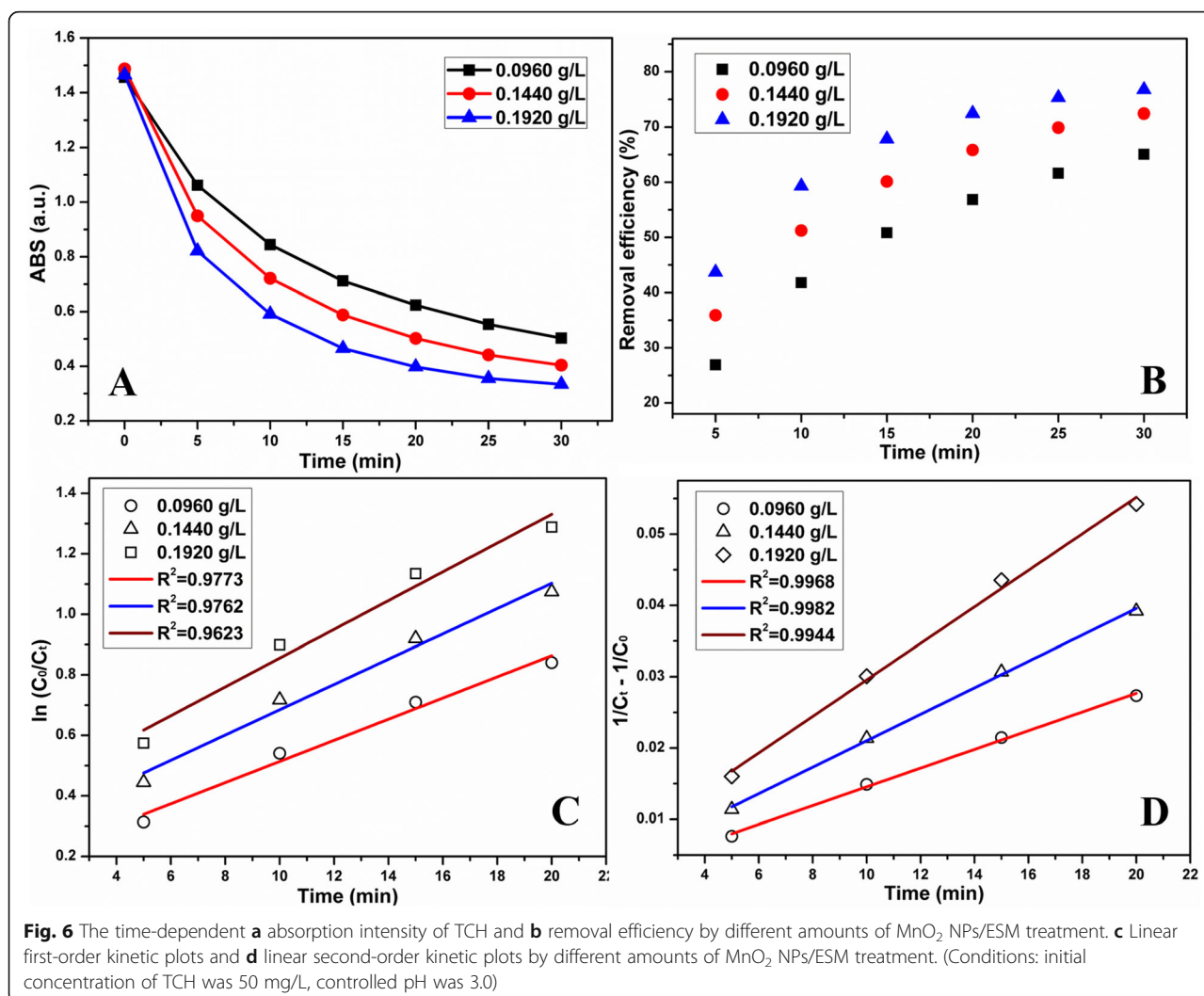


optimal decontamination of TCH by MnO₂ NPs/ESM was achieved under PBS buffer with a pH of 3.0. Moreover, TCH decontamination by MnO₂ NPs/ESM without buffer solution was investigated in Fig. 5c, in which the absorption intensity of TCH decreased gradually and pH of the degradation system was steadily improved. The same phenomenon of pH increase during the decontamination process was also reported in a previous work [38]. It was worth noting that the removal efficiency without buffer increased more rapidly than that under a buffered condition at the beginning (first 20 min). Then as the time passed, however, the removal efficiency with buffer exceeded the one without buffer after 30 min (83.10% for buffered and 78.37% for the unbuffered condition at 60 min). Removal efficiencies were monitored through concentration variations of TCH which were calculated from linear calibration plot (Additional file 6: Figure S6 and Additional file 7: Figure S7). Under the buffered condition, saline ions from PBS hindered the

diffusion of TCH molecules onto the surface of MnO₂ NPs for further reaction, and hence, the reaction rate was lower than that of without a buffer. However, pH increase of reaction system along with time under unbuffered condition limited the oxidative capacity of MnO₂ NPs, and thus, the removal efficiency cannot reach the one obtained under controlled optimal pH.

Kinetic Study of TCH Decontamination

To further understand the TCH degradation by MnO₂ NPs/ESM, the kinetic study was carried out by changing the TCH initial concentration or dose of MnO₂. We investigated the kinetics of degradation by different amounts of MnO₂ under buffered conditions. Figure 6a displayed the time-dependent absorption intensity of TCH degraded by different doses of MnO₂ (0.0960, 0.1440, and 0.1920 g/L), and the corresponding removal efficiencies were calculated in Fig. 6b. And linear kinetic plots by pseudo-first-order and pseudo-second-order



were fitted in Fig. 6c, d, respectively. Moreover, degradation at different initial concentrations of TCH (30, 50, and 70 mg/L) with buffer was studied through monitoring the absorption intensity (Fig. 7a) and removal efficiency (Fig. 7b) at different times. Figure 7c, d fitted the linear first/second-order kinetic plots to investigate the kinetics. Similarly, degradation kinetics at different amounts of MnO₂ NPs and different initial TCH concentrations under unbuffered conditions were studied in Additional file 8: Figure S8 and Additional file 9: Figure S9, respectively. Table 1 exhibited the kinetic data obtained from different conditions. The correlation coefficients were linear-fitted and calculated to demonstrate the kinetic of TCH degradation by MnO₂ NPs/ESM. Generally, the correlation coefficients calculated through the pseudo-second-order model were higher than that through pseudo-first-order, indicating this process was more consistent with the pseudo-second-order model. In detail, this pseudo-second-order model had higher

correlation coefficients at small doses of MnO₂ or high initial concentrations of TCH. And either way, correlation coefficients were closer to 1 in the buffered conditions compared with the degradation without a buffer.

Comparison of Commercial MnO₂ Powder and Other Reported Materials

To illustrate the advanced property of as-prepared MnO₂ NPs/ESM, the equal amount of commercial MnO₂ powder was contrastively tested for TCH decontamination under the same conditions. Figure 8 showed the removal efficiency from as-prepared MnO₂ NPs/ESM and commercial MnO₂ powder with or without a buffer. It was indicated that MnO₂ NPs/ESM showed a prominent advantage over commercial MnO₂ powder under both conditions. Though removal efficiency of around 80% through MnO₂ decontamination was obtained in previous work [38, 39], it could reach up to 98% under pH = 6.5 through a MnO₂ and zero-valent iron (ZVI)-based

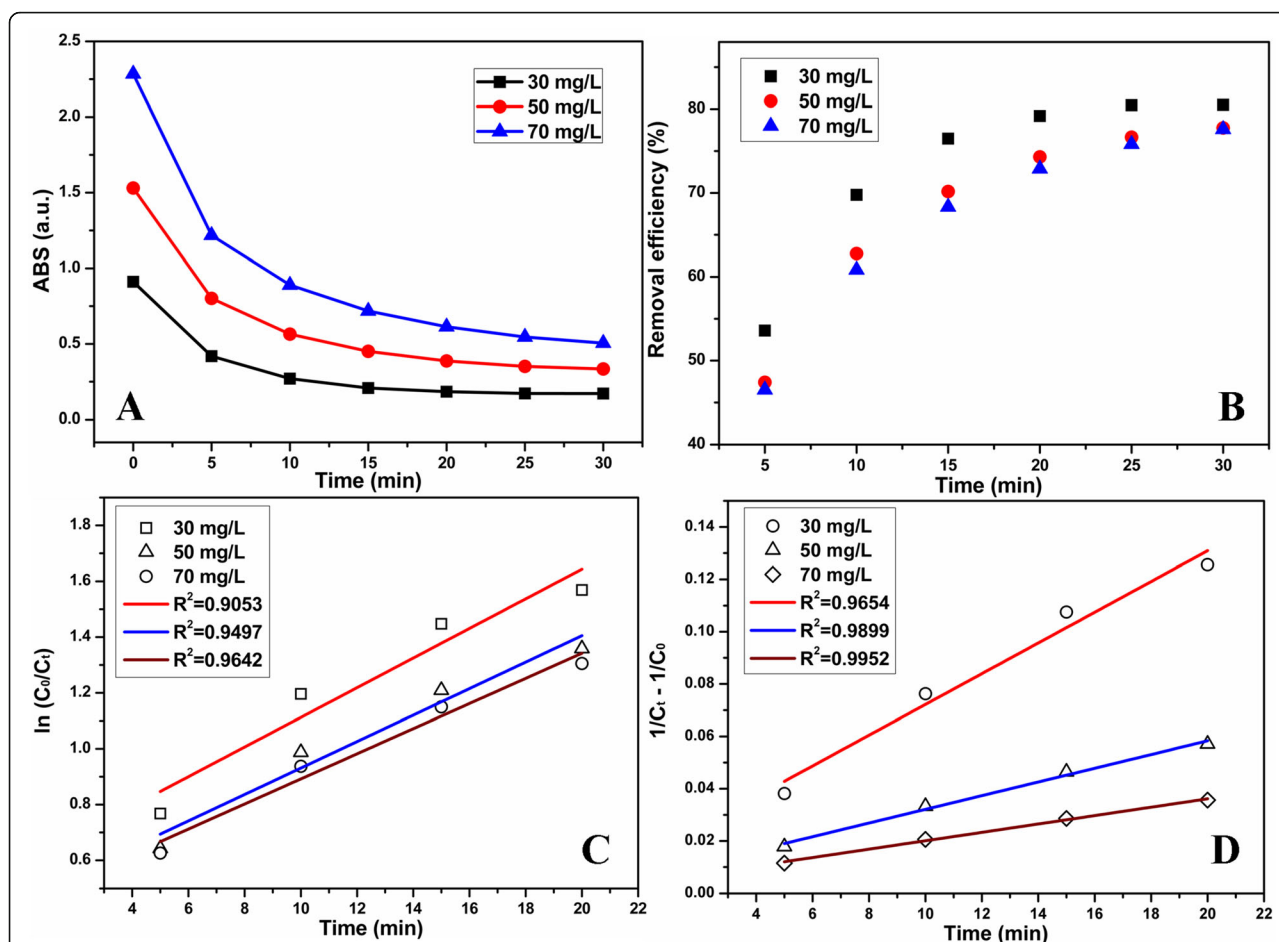


Fig. 7 The time-dependent **a** absorption intensity of TCH and **b** removal efficiency for the degradation of different initial concentrations of TCH. **c** Linear first-order kinetic plots and **d** linear second-order kinetic plots for degradation of different initial concentrations of TCH. (Conditions: a dose of MnO₂ NPs/ESM was 0.1740 g/L, controlled pH was 3.0)

Table 1 The kinetic data under different conditions

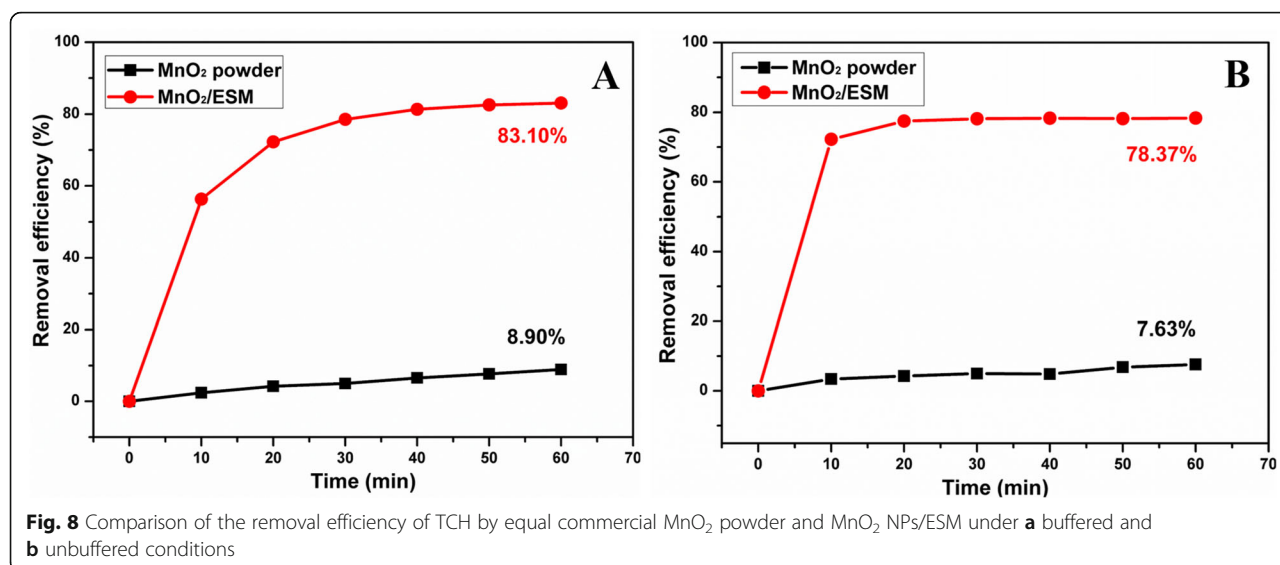
Initial conc. ^a	Dose ^b	Buffer ^c	R^2 (first-order)	R^2 (second-order)
50	0.0960	Yes	0.9773	0.9968
50	0.1440	Yes	0.9762	0.9982
50	0.1920	Yes	0.9623	0.9944
30	0.1920	Yes	0.9053	0.9654
50	0.1920	Yes	0.9497	0.9899
70	0.1920	Yes	0.9642	0.9952
50	0.0960	No	0.9637	0.9841
50	0.1440	No	0.8719	0.9126
50	0.1920	No	0.8558	0.9053
30	0.1920	No	0.8775	0.9330
50	0.1920	No	0.8558	0.9053
70	0.1920	No	0.8896	0.9249

^aInitial concentration of TCH (mg/L)

^bDose of MnO₂ (g/L)

^cPBS buffer (pH = 3.0)

permeable reactive barrier (PRB) system [56], which was attributed to the multiple effects from ZVI coupling with MnO₂. Besides, other materials were also applied to TC decontamination. Immobilized TiO₂ nanobelts modified by Au and CuS nanoparticles (Au–CuS–TiO₂ NBs) displayed a removal efficiency of 96% towards oxytetracycline (OTC) owing to their superior photocatalytic activity [57]. Graphene oxide (GO) as an efficient adsorbent showed a good removal for TC after 24 h ($R = 96\%$) [58]. Powder activated carbon/Fe₃O₄ magnetic nanoparticles (PAC/Fe₃O₄ MNPs) were applied as a catalyst to H₂O₂-assisted TC degradation, and removal efficiency of 94.5% was obtained [59]. It was noticed that the removal efficiency could be enhanced by prolonging the treatment time or increasing the material doses [39]. Nevertheless, all the work needs complicated degradation measurement and subsequent processing which increase the labor and test time. The handy operation of our method such as



neither centrifugation nor filtration would facilitate the decontamination procedure.

Conclusions

MnO_2 nanoparticles were synthesized in this work through a super easy procedure by mixing the eggshell membrane and potassium permanganate solutions. This harsh reaction conditions or complicated aftertreatment needless method made synthesis and purification process quickly and handy. The obtained MnO_2 nanoparticles dispersed uniformly onto the surface of fibrous proteins to form a microcosmic/macrosopic combination mode. Further, the eggshell membrane-templated MnO_2 nanoparticles were applied to tetracycline hydrochloride decontamination. A removal efficiency of 83.10% after 60 min under the buffered condition and pseudo-second-order model kinetics were obtained. Most notably, MnO_2 NPs/ESM can be separated easily by taking it out of the solutions, which avoided complex operation like centrifugation or filtration, making it an advantage in nanomaterial-based wastewater decontamination.

Additional files

Additional file 1: Figure S1. Size distribution of as-prepared MnO_2 NPs. (TIF 168 kb)

Additional file 2: Figure S2. (A) The photos of MnO_2 NPs/ESM before and after NaOH treatment. (B) The photos of filtrated solutions after NaOH treatment from blank ESM and MnO_2 NPs/ESM, respectively. (C) Size distribution of ESM after NaOH treatment. (TIF 1576 kb)

Additional file 3: Figure S3. Contrast pictures of MnO_2 NPs/ESM (A) before reaction, (B) right after immersed into GSH aqueous solution (1 mM) and (C) after 1 min soaking. (TIF 1310 kb)

Additional file 4: Figure S4. The TG curves of ESM (black) and MnO_2 NPs/ESM (red). (TIF 501 kb)

Additional file 5: Figure S5. FTIR spectra of ESM and MnO_2 NPs/ESM with deconvolution. (TIF 1223 kb)

Additional file 6: Figure S6. Linear calibration plot for TCH ranging from 0.1 to 75 mg/L without a buffer. (TIF 165 kb)

Additional file 7: Figure S7. Linear calibration plot for TCH ranging from 0.1 to 75 mg/L with buffer (pH = 3). (TIF 1673 kb)

Additional file 8: Figure S8. Degradation kinetics of TCH at different amounts of MnO_2 NPs/ESM under unbuffered conditions. The time-dependent of absorption intensity of TCH (A), removal efficiency by different amounts of MnO_2 NPs/ESM treatment (B), linear first order kinetic plots (C) and linear second order kinetic plots (D) with different amounts of MnO_2 NPs/ESM treatment. (conditions: initial concentration of TCH was 50 mg/L, without PBS buffer). (TIF 4052 kb)

Additional file 9: Figure S9. Degradation kinetics of TCH at different initial TCH concentration under unbuffered conditions. The time-dependent of absorption intensity of TCH (A) and (B) removal efficiency for degradation of different initial concentrations of TCH. (C) Linear first order kinetic plots and (D) linear second order kinetic plots for degradation of different initial concentrations of TCH. (conditions: dose of MnO_2 NPs/ESM was 0.1740 g/L, without PBS buffer). (TIF 860 kb)

Abbreviations

ESM: Eggshell membrane; GSH: Glutathione; HRTEM: High-resolution transmission electron microscopy; NPs: Nanoparticles; OTC: Oxytetracycline; PBS: Phosphate buffer saline; PPCPs: Pharmaceuticals and personal care products; SEM: Scanning electron microscopy; TCH: Tetracycline hydrochloride; TCs: Tetracyclines; TEM: Transmission electron microscopy; TG: Thermogravimetry; UV-vis: Ultraviolet-visible; XPS: X-ray photoelectron spectroscopy

Acknowledgements

We thank the Institute of Coal Chemistry, Chinese Academy of Science, for the material characterization.

Funding

The present work was supported by the Program for the (Reserved) Discipline Leaders of Taiyuan Institute of Technology.

Availability of Data and Materials

All datasets are presented in the main paper or in the additional supporting files.

Authors' Contributions

QW and LHM designed the experiment. QW and CLM performed the experiments and co-wrote the paper. JKT and CHZ contributed to the data processing. All authors read and approved the final manuscript.

Competing Interests

The authors declare that they have no competing interests.

Publisher's Note

Springer Nature remains neutral with regard to jurisdictional claims in published maps and institutional affiliations.

Author details

¹Chemistry and Chemical Engineering Department, Taiyuan Institute of Technology, Taiyuan 030008, Shanxi, China. ²NMR and Drug Metabolism Core, Baylor College of Medicine, One Baylor Plaza, Houston, TX 77030, USA. ³College of Science and Engineering, University of Houston-Clear Lake, 2700 Bay Area Blvd, Houston, TX 77058, USA.

Received: 3 April 2018 Accepted: 21 August 2018

Published online: 28 August 2018

References

- Richardson SD, Ternes TA (2014) Water analysis: emerging contaminants and current issues. *Anal Chem* 86:2813–2848
- Park J, Yamashita N, Wu G, Tanaka H (2017) Removal of pharmaceuticals and personal care products by ammonia oxidizing bacteria acclimated in a membrane bioreactor: contributions of cometabolism and endogenous respiration. *Sci Total Environ* 605–606:18–25
- Yang Y, Ok YS, Kim KH, Kwon EE, Tsang YF (2017) Occurrences and removal of pharmaceuticals and personal care products (PPCPs) in drinking water and water/sewage treatment plants: a review. *Sci Total Environ* 596–597: 303–320
- Yi X, Tran NH, Yin T, He Y, Gin KY (2017) Removal of selected PPCPs, EDCs, and antibiotic resistance genes in landfill leachate by a full-scale constructed wetlands system. *Water Res* 121:46–60
- Kumar A, Khan M, Fang L, Lo IMC (2017) Visible-light-driven N-TiO₂@SiO₂@Fe₃O₄ magnetic nanophotocatalysts: synthesis, characterization, and photocatalytic degradation of PPCPs. *J Hazard Mater* In press
- Qi N, Wang P, Wang C, Ao Y (2018) Effect of a typical antibiotic (tetracycline) on the aggregation of TiO₂ nanoparticles in an aquatic environment. *J Hazard Mater* 341:187–197
- Palominos RA, Mondaca MA, Giraldo A, Peñuela G, Pérez-Moya M, Mansilla HD (2009) Photocatalytic oxidation of the antibiotic tetracycline on TiO₂ and ZnO suspensions. *Catal Today* 144:100–105
- Li Z, Schulz L, Ackley C, Fenske N (2010) Adsorption of tetracycline on kaolinite with pH-dependent surface charges. *J Colloid Interf Sci* 251:254–260
- Zhao YH, Liu ZL, Li LH, Jiang SH, Shi CH (2012) Systematic review of randomized controlled trials of traditional Chinese medicine treatment of non-acute bronchial asthma complicated by gastroesophageal reflux. *J Tradit Chin Med* 32:12–18
- Di J, Xia J, Ge Y, Li H, Ji H, Xu H, Zhang Q (2015) Novel visible-light-driven CQDs/Bi₂WO₆ hybrid materials with enhanced photocatalytic activity toward organic pollutants degradation and mechanism insight. *Appl Catal B Environ* 182:115–122
- Zhu Z, Lu Z, Wang D, Tang X, Yan Y, Shi W, Wang Y, Gao N, Yao X, Dong H (2016) Construction of high-dispersed Ag/Fe₃O₄/g-C₃N₄ photocatalyst by selective photo-deposition and improved photocatalytic activity. *Appl Catal B Environ* 182:115–122
- Hong Y, Jiang Y, Li C, Fan W, Yan X, Yan M, Shi W (2016) In-situ synthesis of direct solid-state Z-scheme V₂O₅/g-C₃N₄ heterojunctions with enhanced visible light efficiency in photocatalytic degradation of pollutants. *Appl Catal B Environ* 180:663–673
- Lu X, Wang Y, Zhang X, Xu G, Wang D, Lv J, Zheng Z, Wu Y (2018) NiS and MoS₂ nanosheet co-modified graphitic C₃N₄ ternary heterostructure for high efficient visible light photodegradation of antibiotic. *J Hazard Mater* 341:10–19
- Mallakpour S, Motirasoul F (2018) Ultrasonication synthesis of PVA/PVP/α-MnO₂-stearic acid blend nanocomposites for adsorbing Cd^{II} ion. *Ultrason Sonochem* 40:410–418
- Guo Y, Guo H, Wang Y, Liu L, Chen W (2014) Designed hierarchical MnO₂ microspheres assembled from nanofilms for removal of heavy metal ions. *RSC Adv* 4:14048–14054
- Adil SF, Alabbad S, Kuniyil M, Khan M, Alwarthan A, Mohri N, Tremel W, Tahir MN, Siddiqui MRH (2015) Vanadia supported on nickel manganese oxide nanocatalysts for the catalytic oxidation of aromatic alcohols. *Nanoscale Res Lett* 10(51):1–9
- Qian K, Qian Z, Hua Q, Jiang Z, Huang W (2013) Structure-activity relationship of CuO/MnO₂ catalysts in CO oxidation. *Appl Surf Sci* 273:357–363
- Shu Y, Xu J, Chen J, Xu Q, Xiao X, Jin D, Pang H, Hu X (2017) Ultrasensitive electrochemical detection of H₂O₂ in living cells based on ultrathin MnO₂ nanosheets. *Sensor Actuat B Chem* 252:72–78
- Liu C, Navale ST, Yang ZB, Galluzzi M, Patil VB, Cao PJ, Mane RS, Stadler FJ (2017) Ethanol gas sensing properties of hydrothermally grown α-MnO₂ nanorods. *J Alloy Compd* 727:362–369
- Zhang C, Zhu X, Wang Z, Sun P, Ren Y, Zhu J, Zhu J, Xiao D (2014) Facile synthesis and strongly microstructure-dependent electrochemical properties of graphene/manganese dioxide composites for supercapacitors. *Nanoscale Res Lett* 9:490/1–490/8
- Jiang S, Shi T, Hu L, Sun Y, Zhou W, Tang Z (2014) High-performance binder-free supercapacitor electrode by direct growth of cobalt-manganese composite oxide nanostructures on nickel foam. *Nanoscale Res Lett* 9:492/1–492/8
- Zhang M, Xing L, Ke H, He YJ, Cui PF, Zhu Y, Jiang G, Qiao JB, Lu N, Chen H, Jiang HL (2017) MnO₂-based nanoplateform serves as drug vehicle and MRI contrast agent for cancer theranostics. *ACS Appl Mater Inter* 9:11337–11344
- Yang G, Xu L, Chao Y, Xu J, Sun X, Wu Y, Peng R, Liu Z (2017) Hollow MnO₂ as a tumor-microenvironment-responsive biodegradable nano-platform for combination therapy favoring antitumor immune responses. *Nat Commun* 8:902
- Tian L, Chen Q, Yi X, Chen J, Liang C, Chao Y, Yang K, Liu Z (2017) Albumin-templated manganese dioxide nanoparticles for enhanced radioisotope therapy. *Small* 13:1700640/1–1700640/9
- Chu C, Lin H, Liu H, Wang X, Wang J, Zhang P, Gao H, Zeng Y, Tan Y, Liu G, Chen X (2017) Tumor microenvironment-triggered supramolecular system as an in situ nanotheranostic generator for cancer phototherapy. *Adv Mater* 29:1605928/1–1605928/7
- Mallakpour S, Motirasoul F (2017) Bio-functionalizing of α-MnO₂ nanorods with natural L-amino acids: a favorable adsorbent for the removal of Cd(II) ions. *Mater Chem Phys* 191:188–196
- Sun H, Xu K, Huang M, Shang Y, She P, Yin S, Liu Z (2015) One-pot synthesis of ultrathin manganese dioxide nanosheets and their efficient oxidative degradation of rhodamine B. *Appl Surf Sci* 357:69–73
- Saputra E, Muhammad S, Sun H, Patel A, Shukla P, Zhu ZH, Wang S (2012) α-MnO₂ activation of peroxymonosulfate for catalytic phenol degradation in aqueous solutions. *Catal Commun* 26:144–148
- Li Y, Wei D, Du Y (2015) Oxidative transformation of levofloxacin by d-MnO₂: products, pathways and toxicity assessment. *Chemosphere* 119:282–288
- Jalali HM (2016) Kinetic study of antibiotic ciprofloxacin ozonation by MW/CNT/MnO₂ using Monte Carlo simulation. *Mater Sci Eng C* 59:924–929
- Luo Y, Bai B, Wang H, Suo Y, Yao Y (2017) Efficient absorption of antibiotic from aqueous solutions over MnO₂@SA/Mn beads and their in situ regeneration by heterogeneous Fenton-like reaction. *J Nanomater* 4:1–13
- Wan J, Zhou L, Deng H, Zhan F, Zhang P (2015) Oxidative degradation of sulfamethoxazole by different MnO₂ nanocrystals in aqueous solution. *J Mol Catal A Chem* 407:67–74
- Dong J, Li Y, Zhang L, Liu C, Zhuang L, Sun L, Zhou J (2009) The oxidative degradation of sulfadiazine at the interface of α-MnO₂ and water. *J Chem Technol Biotechnol* 84:1848–1853
- Li L, Wei D, Wei G, Du Y (2017) Product identification and the mechanisms involved in the transformation of cefazolin by birnessite (δ-MnO₂). *Chem Eng J* 320:116–123
- Chen WR, Ding Y, Johnston CT, Teppen BJ, Boyd SA, Li H (2010) Reaction of lincosamide antibiotics with manganese oxide in aqueous solution. *Environ Sci Technol* 44:4486–4492
- Rubert KF, Pedersen JA (2006) Kinetics of oxytetracycline reaction with a hydrous manganese oxide. *Environ Sci Technol* 40:7216–7221
- Zhang H, Chen WR, Huang CH (2008) Kinetic modeling of oxidation of antibacterial agents by manganese oxide. *Environ Sci Technol* 42:5548–5554
- Mahamallik P, Saha S, Pal A (2015) Tetracycline degradation in aquatic environment by highly porous MnO₂ nanosheet assembly. *Chem Eng J* 276:155–165
- Wang H, Zhang D, Mou S, Song W, Al-Misned FA, Mortuza MG, Pan X (2015) Simultaneous removal of tetracycline hydrochloride and As(III) using poorly-crystalline manganese dioxide. *Chemosphere* 136:102–110

40. Chen G, Zhao L, Dong YH (2011) Oxidative degradation kinetics and products of chlortetracycline by manganese dioxide. *J Hazard Mater* 193:128–138
41. Baláz M (2014) Eggshell membrane biomaterial as a platform for applications in materials science. *Acta Biomater* 10:3827–3843
42. Devi PS, Banerjee S, Chowdhury SR, Kumar GS (2012) Eggshell membrane: a natural biotemplate to synthesize fluorescent gold nanoparticles. *RSC Adv* 2: 11578–11585
43. Zheng BZ, Xie SP, Qian L, Yuan HY, Xiao D, Choi MMF (2011) Gold nanoparticles-coated eggshell membrane with immobilized glucose oxidase for fabrication of glucose biosensor. *Sensor Actuat B* 152:49–55
44. Liang M, Su R, Qi W, Yu Y, Wang L, He Z (2014) Synthesis of well-dispersed Ag nanoparticles on eggshell membrane for catalytic reduction of 4-nitrophenol. *J Mater Sci* 49:1639–1647
45. Dong Q, Su HL, Song F, Zhang D, Wang N (2007) Hierarchical metal oxides assembled by nanocrystallites via a simple bio-inspired route. *J Am Ceram Soc* 90:376–380
46. Mallampati R, Valiyaveetil S (2012) Simple and efficient biomimetic synthesis of Mn_2O_3 hierarchical structures and their application in water treatment. *J Nanosci Nanotechnol* 12:618–622
47. Camaratta R, Lima ANC, Reyes MD, Hernandez-Fenollosa MA, Messina JO, Bergmann CP (2013) Microstructural evolution and optical properties of TiO_2 synthesized by eggshell membrane templating for DSSCs application. *Mater Res Bull* 48:1569–1574
48. Tan XQ, Wan YF, Huang YJ, He C, Zhang ZL, He ZY, Hu LL, Zeng JW, Shu D (2017) Three-dimensional MnO_2 porous hollow microspheres for enhanced activity as ozonation catalysts in degradation of bisphenol A. *J Hazard Mater* 321:162–172
49. Xu Y, Chen X, Chai R, Xing C, Li H, Yin XB (2016) A magnetic/fluorometric bimodal sensor based on a carbon dots– MnO_2 platform for glutathione detection. *Nanoscale* 8:13414–13421
50. Dong ZZ, Lu L, Ko CN, Yang C, Li S, Lee MY, Leung CH, Ma DL (2017) A MnO_2 nanosheet-assisted GSH detection platform using an iridium(III) complex as a switch-on luminescent probe. *Nanoscale* 9:4677–4682
51. Hashem AM, Abuzeid H, Kaus M, Indris S, Ehrenberg H, Mauger A, Julien CM (2018) Green synthesis of nanosized manganese dioxide as positive electrode for lithium-ion batteries using lemon juice and citrus peel. *Electrochim Acta* 262:74–81
52. Hashem AM, Abdel-Latif AM, Abuzeid HM, Abbas HM, Ehrenberg H, Farag RS, Mauger A, Julien CM (2011) Improvement of the electrochemical performance of nanosized $\alpha\text{-MnO}_2$ used as cathode material for Li-batteries by Sn-doping. *J Alloy Compd* 509:9669–9674
53. Liu X, Wang Q, Zhao HH, Zhang LC, Su YY, Lv Y (2012) BSA-templated MnO_2 nanoparticles as both peroxidase and oxidase mimics. *Analyst* 137: 4552–4558
54. Dubal DP, Kim WB, Lokhande CD (2011) Surfactant assisted electrodeposition of MnO_2 thin films: improved supercapacitive properties. *J Alloy Compd* 509:10050–10054
55. Chacón-Patiño ML, Blanco-Tirado C, Hinestroza JP, Combariza MY (2013) Biocomposite of nanostructured MnO_2 and fique fibers for efficient dye degradation. *Green Chem* 15:2920–2928
56. Dong GH, Huang LH, Wu XY, Wang C, Liu YY, Liu GF, Wang LS, Liu XW, Xia HB (2018) Effect and mechanism analysis of MnO_2 on permeable reactive barrier (PRB) system for the removal of tetracycline. *Chemosphere* 193:702–710
57. Chen QH, Wu SN, Xin YJ (2016) Synthesis of Au–CuS– TiO_2 nanobelts photocatalyst for efficient photocatalytic degradation of antibiotic oxytetracycline. *Chem Eng J* 302:377–387
58. Yang YX, Hu XJ, Zhao YL, Cui LH, Huang ZJ, Long JL, Xu JW, Deng JB, Wu CY, Liao WW (2017) Decontamination of tetracycline by thiourea-dioxide-reduced magnetic graphene oxide: effect of pH, ionic strength, and humic acid concentration. *J Colloid Interf Sci* 495:68–77
59. Jaafarzadeh N, Kakavandi B, Takdastan A, Kalantary RR, Azizi M, Jorfi S (2015) Powder activated carbon/ Fe_3O_4 hybrid composite as a highly efficient heterogeneous catalyst for Fenton oxidation of tetracycline: degradation mechanism and kinetic. *RSC Adv* 5:84718–84728

Submit your manuscript to a SpringerOpen[®] journal and benefit from:

- Convenient online submission
- Rigorous peer review
- Open access: articles freely available online
- High visibility within the field
- Retaining the copyright to your article

Submit your next manuscript at ► [springeropen.com](https://www.springeropen.com)